J Neuropathol Exp Neurol
Vol. 69, No. 3
March 2010
pp. 281–293

ORIGINAL ARTICLE

Motor Axonal Sprouting and Neuromuscular Junction Loss in an Animal Model of Charcot-Marie-Tooth Disease

Eng-Tat Ang, PhD, Ralf Schäfer, PhD, Richard Baltensperger, PhD, Anton Wernig, MD, PhD, Marco Celio, MD, and Sara Sancho Oliver, MD, PhD

Abstract

Muscle weakness in Charcot-Marie-Tooth Type 1A disease (CMT1A) caused by mutations in peripheral myelin protein 22 (PMP22) has been attributed to an axonopathy that results in denervation and muscle atrophy. The underlying pathophysiological mechanisms involved are not understood. We investigated motor performance, neuromuscular junctions (NMJs), physiological parameters, and muscle morphometry of PMP22 transgenic mice. Neuromuscular junctions were progressively lost in hindlimb muscles of PMP22 transgenic mice, but their motor performance did not completely deteriorate during the observation period. There was considerable variability, including in laterality, in deficits among the animals. Cross-sectional areas and mean fiber size measurements indicated variable myofiber atrophy in hindlimb muscles. There was substantial concomitant axonal sprouting, and loss of neuromuscular junctions was inversely correlated with the accumulated length of axonal branches. Synaptic transmission studied in isolated nerve/muscle preparations indicated variable partial muscle denervation. Acetylcholine sensitivity was higher in the mutant muscles, and maximum tetanic force evoked by direct or indirect stimulation, specific force, and wet weights were markedly reduced in some mutant muscles. In summary, there is partial muscle denervation, and axons may retain some regenerative capacity but fail to reinnervate muscles in PMP22 transgenic mice.

Key Words: Animal model, Axon sprouting, Charcot-Marie-Tooth disease, Muscle fiber morphometry, Neuromuscular junction, PMP22, Synaptic transmission.

INTRODUCTION

Charcot-Marie-Tooth disease (CMT) is one of the most prevalent inherited neurological disorders, with an estimated occurrence of 1 in 2,500 (1). Importantly, it can affect the quality of life of patients (2). Numerous genes are implicated in the variable clinical phenotypes of CMT. Mutations of peripheral myelin protein 22 (PMP22), a structural component of myelin of the peripheral nervous system (PNS), are responsible for CMT Type 1A (CMT1A). The most frequent genetic abnormality that causes CMT1A is a partial duplication on the short arm of chromosome 17, which results in PMP22 trisomy (3, 4). Many patients with the chromosome 17p11.2 duplication develop the classic CMT phenotype characterized by a slowly progressive symmetrical motor and sensory polyneuropathy with onset in childhood or adolescence. Patients have variable degrees of distal weakness, muscle atrophy, and sensory deficits (5). Furthermore, they often present with a foot drop, poor biomechanics, and hence, poor balance (6). The neuropathy is primary demyelinating, with marked slowing of nerve conduction velocity that can be detected years before the disease becomes clinically apparent (7, 8). Occasionally, a PMP22 point mutation rather than duplication is found in CMT1A patients (9, 10). In general, PMP22 point mutations cause the allelic disorders Dejerine-Sottas syndrome and congenital hypomyelination, diseases that exhibit a more severe clinical course than classical CMT (11).

Nerve biopsies of CMT1A are characterized by segmental demyelination, remyelination, and onion bulbs formed by redundant concentric Schwann cell (SC) lamellae (12, 13). Loss of myelinated fibers and reduced axonal diameters are common findings, but evidence of active axonal degeneration and clusters of regenerating axons is rare (14). There are numerous studies of nerve biopsies of CMT patients, but there is only limited information regarding skeletal muscle pathology. When muscle biopsies were performed, however, they showed typical neuropathic features (15).

Animal models have proven valuable to further our understanding of the genetics, genotype/phenotype correlations, and disease mechanisms of CMT. For example, several lines of transgenic (Tg) mice (16–18) and rats (19) that carry additional copies of the *PMP22* gene implicated it as the gene responsible for CMT1A; they also have demonstrated that the disease is gene dosage sensitive. The phenotype of these genetically modified animals mimics many hallmarks of the human disease including poor gait and balance. The PMP22-Tg animals with low copy numbers of a *pmp22* transgene develop a demyelinating peripheral neuropathy, whereas animals carrying high copy numbers make little or no myelin in the PNS (16–20). The PMP22-deficient mice have delayed

From the Department of Medicine/Unit of Anatomy, Faculty of Science, University of Fribourg, Fribourg, Switzerland (E-TA, MC, SSO); Department of Physiology II, Faculty of Medicine, University of Bonn, Bonn, Germany (RS, AW); and Ecole d'ingénieurs et d'architectes de Fribourg, Fribourg, Switzerland (RB).

Send correspondence and reprint requests to: Marco Celio, MD, University of Fribourg, Department of Medicine, Anatomy unit, 1, Rte. Albert Gockel, CH-1700 Fribourg, Switzerland; E-mail: marco.celio@unifr.ch

Supplemental digital content is available for this article. Direct URL citations appear in the printed text and are provided in the HTML and PDF versions of this article on the journal's Web site (www.jneuropath.com).

myelination, followed by hypermyelination, and subsequent segmental demyelination (21).

In addition to myelin defects, CMT1A animal models develop a distal axonopathy. Large-caliber axons are absent, and total numbers of myelin-competent axons are decreased in the PNS of aged PMP22-deficient and PMP22-Tg mice. Moreover, ultrastructural evidence of axonal damage is occasionally encountered in PMP22-deficient mice (22). Compelling evidence for a fiber length–related axonopathy has also been revealed in myelin protein zero (P0/MPZ)–deficient mice, a model for CMT1B (23). As in CMT1A patients, skeletal muscles of PMP22-mutant animals show features of denervation (17, 21).

It is now widely accepted that a length-related axonopathy is responsible for many clinical manifestations of CMT1A and other myelin-related CMT subtypes, but how this axonopathy develops and leads to neurogenic muscle atrophy is not understood. Interestingly, in a mouse model of hypomyelination, retraction and regeneration of dysfunctional synaptic terminals in the muscle can develop before axonal loss is established at the level of the peripheral nerve trunks (24). There is also evidence for continual remodeling of NMJs on a small scale during ontogeny (25), and dysfunction of synaptic transmission causes enhancement of this remodeling (26, 27).

An earlier study of muscle innervation in the Trembler mouse demonstrated profound modifications of NMJ morphology, marked intramuscular nerve sprouting, and myofiber atrophy, but it did not demonstrate overt denervation of muscle fibers (28). Similar alterations were noticed in muscles of PMP22-Tg mice (29). These findings are at odds with the prevailing view that axonal loss is a main contributor to disease progression in CMT mouse models. Those previous observations were, however, strictly qualitative. To clarify this issue, we performed a longitudinal quantitative study of muscle innervation in PMP22-Tg mice and assessed its impact on motor performance.

MATERIALS AND METHODS

Animals and Genotypic and Phenotypic Analyses

The *thy1*-YFP-16 and *thy1*-YFP-2 mice were purchased from the Jackson Laboratory (Bar Harbor, ME), and the tgN248 of PMP22-Tg (PMP22-Tg) mice were a gift from Professor Ueli Suter (Institute of Cell Biology, ETH-Hönggerberg, Switzerland). The latter line harbors approximately 16 copies of a rodent *pmp22* transgene. The *thy1*-YFP-16 and *thy1*-YFP-2 lines express yellow fluorescent protein (YFP) in all and a subset of neurons, respectively (30). Double-mutant mice (termed PMP22-Tg, *thy1*-YFP-16 and PMP22-Tg, *thy1*-YFP-2) obtained by crossing hemizygous PMP22 Tg females with hemizygous *thy1*-YFP-16 and *thy1*-YFP-2 males were bred and maintained in the animal facility of the Institute of Histology, University of Fribourg, Fribourg, Switzerland. The PMP22 wild-type hemizygous *thy1*-YFP-16 (termed *thy1-YFP-16*) and hemizygous *thy1*-YFP-2 (termed *thy1-YFP-2*) littermates were used as controls.

The YFP genetic status of each mouse was determined by polymerase chain reaction of genomic DNA, as previously described (30). The forward and backward primers were: 5′-AAGTTCATCTGCACCACCG-3′ and 5′-TCCTTGAAGAA GATGGTGCG-3′, respectively. The phenotype of the double mutants was determined by a simple behavioral test: while the animal was held by its tail, persistent flexion of the hindlimbs indicated that it was a PMP22-Tg mouse. In addition, PMP22 double mutants develop clinical signs from about 8 weeks of age, with uncontrolled trembling, unsteady gait, and loss of muscle strength. All experiments were carried out in accordance with guidelines set by the animal research ethics committee (Canton of Fribourg, Fribourg, Switzerland). A time scale of the sequence of experiments is shown in Figure, Supplemental Digital Content 1, http://links.lww.com/NEN/A87.

Muscle Biopsy

For the muscle innervation study, PMP22-Tg, *thy1*-YFP-16 and *thy1*-YFP-16 mice aged 9, 16, and 24 weeks (n = 6 each) were anesthetized with sodium pentobarbital (0.2 mg/g of body weight) via intraperitoneal injection before undergoing transcardiac perfusion with PBS followed by 2% paraformaldehyde. The extensor digitorum longus (EDL) and soleus muscles were removed and injected with Alexa 647–conjugated α-bungarotoxin (α-BTX; Molecular Probes, Eugene, OR) (1:200 in 1% bovine serum albumin in PBS in situ before further incubation in the same preparation (1:1000 dilution) for 1 hour. The muscles were postfixed for another 2 hours at 4°C before teasing and whole mounted onto slides with antifade solution (Molecular Probes). The slides were stored in −20°C until the analysis began.

Confocal Microscopy

All samples were viewed with a Nikon Eclipse E800 microscope and then on a BioRad MRC1024 confocal scanning laser system installed on it with a krypton/argon laser. Image stacks of the entire muscle containing nerve terminals, NMJs, and nerve sprouts were collected with a 10× objective (NA, 0.45) for volume estimation of muscle innervation. Microscopic fields were randomly chosen within the same innervated regions for axonal sprout measurements and NMJ profiling (5 and 8 fields, respectively). Image stacks were collected using either a 20× objective (NA, 0.75) for axonal sprout measurements or a 40× objective (NA, 0.95) for NMJ profiling. Images were obtained using BioRad LaserSharp 2000 software, and all were normalized for laser illumination, iris, gain, and offset levels. Subsequently, all images were managed with Imaris software (Version 4.1; Bitplane, Zurich, Switzerland) to reconstruct z-series images into maximum-intensity projections. Finally, these processed images were enhanced with either Imaris software or Adobe Photoshop CS2 (version 9.0.2; Adobe Systems, Foster City, CA) software for high-quality images.

NMJ Profiling

The NMJs from the double mutants and control muscles were analyzed, tabulated, and scored according to the relationship between the intrasynaptic axonal branches and the postsynaptic membrane assessed by α-BTX staining (24). The NMJs were classified into 4 categories (i.e. normal,

vacant, partially vacant, and sprouting) via imagery using Imaris software. The density was calculated from the total number of NMJs that were recognizable as having pretzel-like α-BTX staining of the postsynaptic apparatus within the volume of muscle analyzed. Small not connected acetylcholine receptor (AChR) aggregates were not quantified. Normal, vacant, partially vacant, and sprouting NMJs were expressed as a percentage of the total number of NMJs counted per muscle and animal.

Axonal Sprouts

Axonal sprouts were analyzed with a design-based stereology paradigm using the *space ball*, otherwise known as the *sphere* (31, 32). Briefly, each 50-μm-thick stack of confocal images was merged and opened with the stereology software (Stereo-Investigator, Version 6.55.1; MicroBrightField, Inc, Williston, VT). The regions of interest (ROI) were closely delineated along the tracing window and typically covered an area of approximately 2×10^5 μm^2. The derived volume by planimetry was therefore 10^7 μm^3. Hemispheres with radii of 20 μm were systematically and randomly placed within the stack of images through the ROI. The parameters for the grid were x, 100 μm; y, 100 μm; guard zone, 5 μm above and below the sphere. The grid rotation was always randomized each time before running the probe. The estimated axonal sprouts were obtained from the total number of intersections between the hemispheres, the presynaptic and intrasynaptic terminal axons, and the sprouts (excluding the nerve bundle) within the ROI.

An estimate of the muscle volume containing terminal axons, NMJs, and sprouts was made for half of the muscle samples using the Cavalieri estimator (32) at every fifth section of the original stack with the size of voxel in the z axis as 6.26 μm. This ROI comprised all regions of the muscle where the aforementioned structures were found and was defined by analogy to the ROI used to estimate the axonal sprouts. Taken together, the final estimated axonal sprouts value in the ROI is obtained by the following equation:

$$[\text{Estimated axonal sprouts in ROI}(\mu\,\text{m}) \div \text{Volume of ROI by planimetry}(\mu\,\text{m}^3)] \times \text{Estimated muscle volume}(\mu\,\text{m}^3).$$

Synaptic Transmission and Contractile Properties of Soleus Muscles

The isometric contractile properties of 8 soleus muscles from 4 experimental (PMP22-Tg *thy1*-YFP-2, n = 3; PMP22-Tg, n = 1) and 10 soleus muscles from 5 control mice (*thy1*-YFP-2, n = 3; wild type mice, n = 2) between 6 and 8 months old were monitored according to previously described protocols (33, 34). Briefly, both soleus muscles with their supplying nerves were surgically removed from animals under neurolept analgesia intraperitoneal injections of 0.4 mg kg^{-1} fentanyl (Fentanyl-Janssen; Janssen, Neuss, Germany), 10 mg kg^{-1} droperidol (Dehydrobenzperidol; Janssen), and 5 mg kg^{-1} diazepam (Valium 10 Roche; Roche, Grenzach-Wyhlen, Germany), and stored in aerated Tyrode solution (125 mmol/L NaCl, 1 mmol/L $MgCl_2$, 1.8 mmol/L $CaCl_2$, 5.4 mmol/L KCl, 24 mmol/L $NaHCO_3$, and 10 mmol/L glucose) until further use. The nerve-muscle preparations were mounted in a horizontal lucite chamber that was continuously perfused with buffered and warmed (25°C ± 0.5°C) Tyrode solution aerated with a gas mixture of 95% vol/vol O_2 and 5% vol/vol CO_2 to prevent O_2 deficits and to maintain the pH at 7.2 to 7.3. The distal (Achilles) tendon of the muscle was connected to a force transducer (DMS 1,5/350LY41; Hottinger Baldwin Messtechnik, Darmstadt, Germany). The proximal tendon was tied to a metal hook firmly attached to the chamber wall. Muscles were adjusted to optimal length (i.e. tension under which standard pulses caused the highest response) and were either stimulated directly with electrical pulses via silver electrodes in the bath (direct stimulation, pulses of 0.5 milliseconds, typically 25 V) or via a suction electrode applied to the ischiadic or soleus nerve (indirect stimulation, 0.1 millisecond, 6 V). For both direct and indirect muscle stimulation, stimulus voltage was set to twice the value sufficient to evoke maximum twitch responses. The variables measured included isometric twitch and tetanic (100 Hz for 2 seconds) tension, the sequence of stimulations was 5 consecutive twitch every 15 seconds, single tetanus (100 Hz for 2 seconds), single twitch, and a train of 4 single twitches (1 Hz). In each set, muscles were first directly stimulated, followed by nerve stimulation after a rest period of 3 minutes. Finally, muscles were stimulated directly with 100 Hz for 2 seconds, and acetylcholine (ACh) sensitivity was tested by rapid exchange of the normal perfusion solution with Tyrode solution containing 0.2 mmol/L ACh perchlorate (Sigma-Aldrich, Germany). After the ACh sensitivity measurement, the muscle chamber was perfused with normal Tyrode solution for 15 minutes. Values for single twitch, tetanus, and ACh contracture were determined from the maximum amplitude, that is, the maximum deviation from the defined baseline observed during event-related force transduction. Specific force was calculated as a ratio of maximum tetanic force to wet muscle weight. Acetylcholine contracture amplitudes were set into relation to the wet weight of the muscle (ACh mg^{-1}). This technique is somewhat more reliable than relating to maximum tetanic tension. Specifically, some chronically denervated, especially thin muscle fibers might escape activation by short electrical pulses applied, but they are activated by bath with ACh and contribute to overall wet weight. Upon completion of the tension recordings, the muscles were weighed, fixed at resting length on pieces of prefixed turkey liver, and were frozen in isopentane cooled in liquid N_2.

Muscle Histology and Quantification

Ten-micrometer cross sections were cut from the midportion of the soleus muscles. Unfixed sections were stained with aqueous toluidine blue–borax solution (both at 1% wt/vol) to reveal the general morphology. These sections were viewed online on a computer monitor through a digital camera (MicroFire-Model S99808; Optronics, Goleta, CA) mounted on an Axioplan microscope (Zeiss AG, Switzerland) equipped with an x/y/z movement-sensitive stage. Muscle area, total number of muscle fiber profiles, and muscle fiber size were

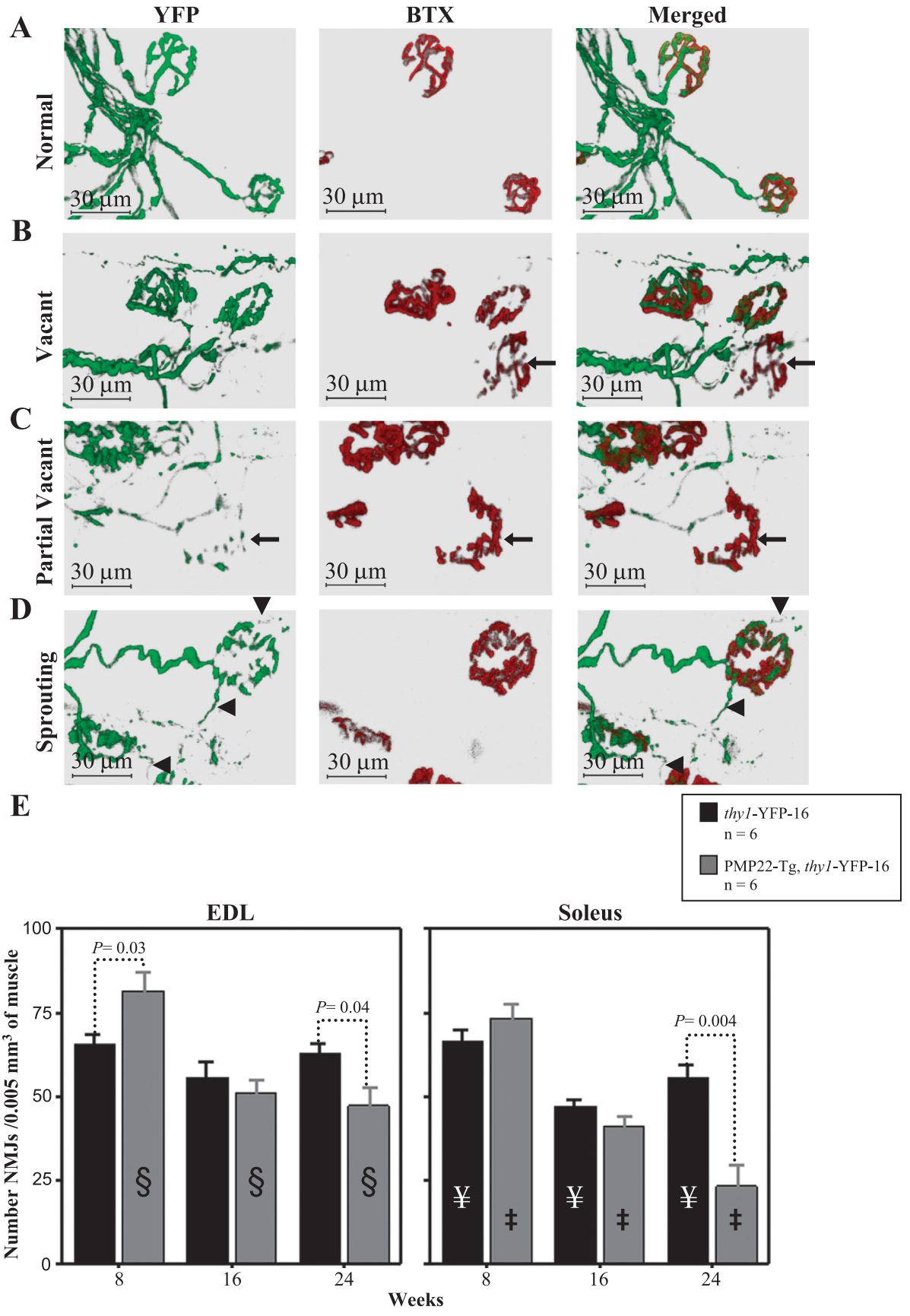

TABLE 1. No. NMJs Examined and Percent Distribution of NMJ Phenotype

Muscle (Genotype) Age, Week	Total NMJs Examined	Normal NMJs (Mean ± SE), %	Vacant NMJs (Mean ± SE), %	Partially Vacant NMJs (Mean ± SE), %	Sprouting NMJs (Mean ± SE), %	NMJs With Subtle Defects (Mean ± SE), %
EDL (*thy1*-YFP-16)						
Week 8	394	84 ± 2.5	0	2.5 ± 1.2	1.2 ± 0.4	13 ± 2.9
Week 16	334	86 ± 5.3	0	0.5 ± 0.5	0	13.8 ± 5.6
Week 24	378	88 ± 3.1	0	3.7 ± 0.6	1.8 ± 1.5	7.3 ± 2.8
EDL (PMP22-Tg, *thy1*-YFP-16)						
Week 8	489	14 ± 6.9*	2.2 ± 0.9†	9.7 ± 1.5†	18 ± 4.6†	56.2 ± 9.5*
Week 16	306	31 ± 8.1*	1.2 ± 0.5	2.7 ± 1.1	23 ± 6†	42.5 ± 2.1†
Week 24	283	6 ± 2.8*	8.2 ± 4.5*	6.2 ± 1.7	45 ± 5.7*	34.7 ± 5.9†
Soleus (*thy1*-YFP-16)						
Week 8	398	80 ± 3.5	1.2 ± 0.8	4.2 ± 1.5	2.7 ± 1.5	12.3 ± 3.7
Week 16	282	91 ± 3.6	0.8 ± 0.5	0	0	8 ± 3.9
Week 24	333	88 ± 5.1	0.5 ± 0.5	2.3 ± 1.1	1.3 ± 1.3	8 ± 5.1
Soleus (PMP22-Tg, *thy1*-YFP-16)						
Week 8	440	5 ± 4*	0.8 ± 0.4	6.2 ± 1.5	35 ± 5.9*	52.8 ± 7.3*
Week 16	245	3 ± 2.7*	0.7 ± 0.7	2.7 ± 1.5	74 ± 3.7*	20.8 ± 6
Week 24	139	0*	0	5.5 ± 3.5	94 ± 3.7*	1.8 ± 1.8

Mice of the indicated genotype (n = 6/group) were examined.
Mann-Whitney U test for PMP22-Tg, *thy1*-YFP-16 versus *thy1*-YFP-16.
*$p < 0.01$; †$p < 0.05$.
EDL, extensor digitorum longus; NMJ, neuromuscular junction.

quantified with the StereoInvestigator software. Muscle area was obtained by tracing the contour of the muscle section that defined the ROI. Total number of muscle profiles and muscle fiber cross-sectional areas were estimated by running the fractionator probe in conjunction with the nucleator probe through the ROI under a 40× objective.

Rotarod Test

The PMP22-Tg, *thy1*-YFP-16 (n = 12) and *thy1*-YFP-16 (n = 10) mice were subjected to the rotarod test. The rotarod unit (TSE Systems GmbH, Bad Homburg, Germany) was linked to a PC running the generic Rotarod software (Version 2.6). In this test which lasted for 24 weeks, we adapted a previously used protocol (35). Each mouse underwent the same 5-day procedure when they were 9, 16, and 23 weeks old. The first 3 days were used to train the animals (training phase). A total of 5 sessions of 120 seconds were run at a very low speed, that is, 5 rotations per minute until a steady baseline level was reached in the performance. The last 2 days were used to run the test sessions (test phase). For this, the mice had to perform 2 sessions per day, each session consisting of 3 trials with 1-hour interval between sessions and a 10-minute rest period between consecutive trials. For each trial, the mouse was placed on the rod, and the rotation speed accelerated from 0 to 36 rotations per minute. The test was ended when the mouse fell from the rod or a maximum of 300 seconds was reached. The latency to fall for all mice was tabulated and compared between the 2 groups at different time points (ninth vs 16th vs 23rd week) (Figure, Supplemental Digital Content 1, http://links.lww.com/NEN/A87).

Statistics

Nonparametric tests were performed in the morphometry and behavior studies with the SPSS software (Version 12.0.1; SPSS Inc, Chicago, IL). A Mann-Whitney U test was used for comparison between 2 groups, and the Kruskal-Wallis test was used when there were more than 2 groups. Attempts to establish correlation between 2 variables were conducted using the Spearman rank correlation coefficient *r*. A *t*-test was applied for the physiology measurements. Values of $p < 0.05$ were considered significant for all tests.

RESULTS

NMJ Profiling and Quantification

NMJs were quantified in a specific volume of soleus and EDL in the double mutants and controls aged 9, 16 and 24 weeks before and after the rotarod test. The soleus, a

FIGURE 1. Representative 2-dimensional images of neuromuscular junctions (NMJs) with diverse morphologies. **(A)** Two normal NMJs. **(B)** A vacant NMJ (arrow) and 2 normal NMJs. **(C)** A partially vacant NMJ with fragmented intrasynaptic branches (arrow). **(D)** Two NMJs with terminal sprouts (arrowheads). Green, yellow fluorescence protein (YFP)–labeled axons; red, Alexa 647 α-bungarotoxin (BTX) to label acetylcholinesterase receptors on muscle fibers. **(E)** Loss of NMJs in PMP22-Tg mouse muscles. The numbers of NMJs in the PMP22-Tg, *thy1*-YFP-16 soleus (n = 6) and extensor digitorum longus (EDL) (n = 6) were declining during the study period as ($^{§}p = 0.005$; $^{‡}p = 0.002$). The *thy1*-YFP-16 muscles did not show this trend. The muscles of 8-week-old PMP22-Tg, *thy1*-YFP-16 mice have a higher density of NMJs than controls, which was significant only for the EDL. Decrease of NMJ density was significant in EDL and soleus of 24-week-old PMP22-Tg, *thy1*-YFP-16 mice compared with controls. Values are presented as mean ± SE.

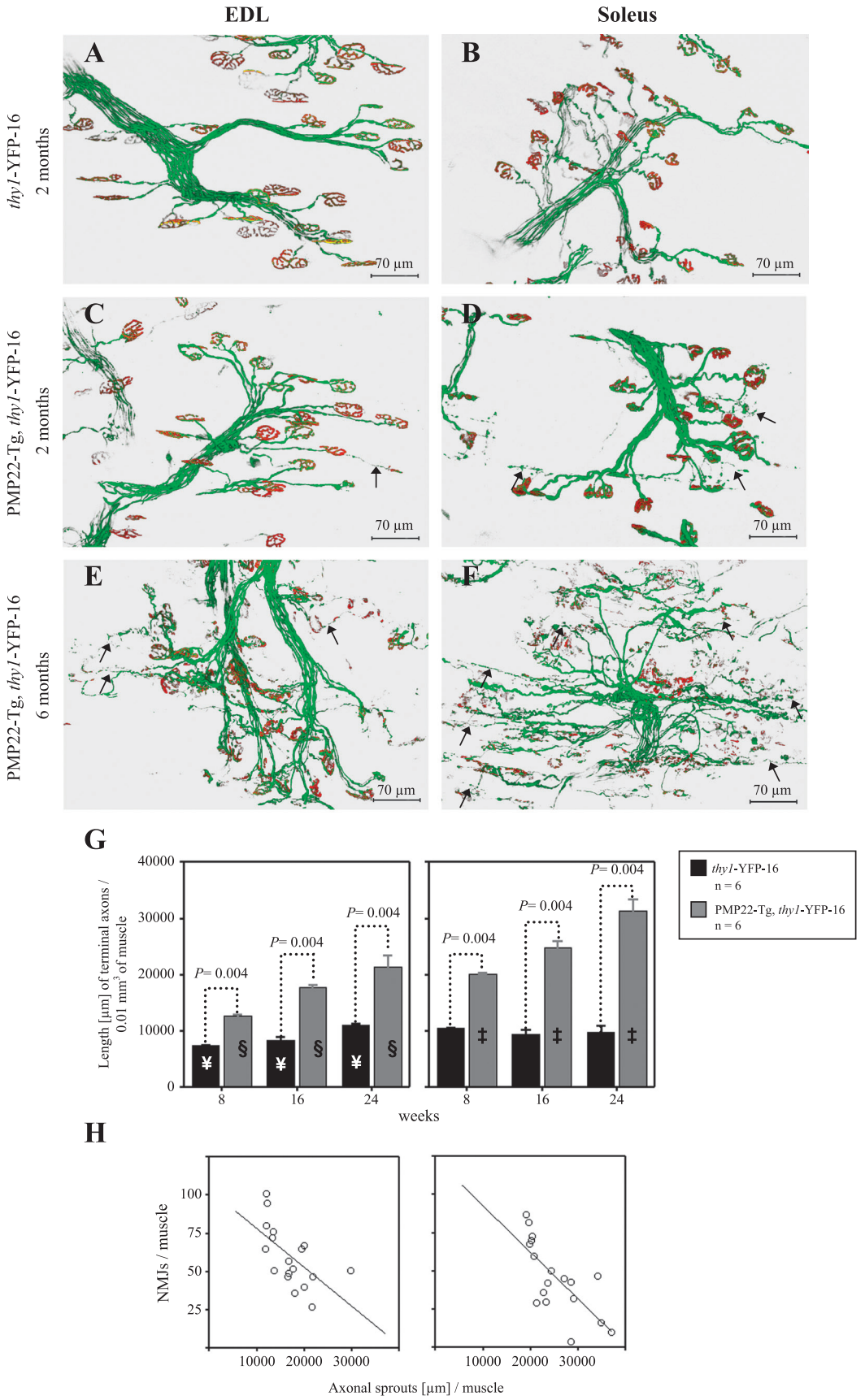

slow-twitch muscle, and the EDL, a fast-twitch muscle, differ in the development (36) and vulnerability to NMJ disassembly and nerve sprouting capability (37).

All identified junctions within the ROI were classified and scored in 4 categories (Fig. 1). Normal NMJs have α-BTX staining with a pretzel-like profile and synaptic terminal branches closely apposed to AChR-rich sites (Fig. 1A). In addition, they should not receive or extend sprouts. Junctions with minor structural changes such as weak or focally patchy α-BTX staining were considered normal. Vacant NMJs were recognized by an α-BTX pretzel-like profile but absence of a nerve in contact with the postsynaptic membrane; they were, therefore, considered denervated (Fig. 1B). Partially vacant NMJs showed α-BTX–labeled postsynaptic sites focally devoid of or containing fragmented nerve terminals (Fig. 1C). Regardless of their morphology, junctions that either received or projected axonal sprouts were scored as sprouting (Fig. 1D).

At age 8 weeks, the density of NMJs was slightly higher in the EDL ($p = 0.03$, Mann-Whitney U test) and to less extent in the soleus of double-mutant mice than in the muscles of age-matched controls (Fig. 1E). This suggests the presence of atrophic muscle fibers in the mutants. During the study period, the numbers of NMJs per ROI significantly decreased in double-mutant animals (EDL, $p = 0.005$; soleus, $p = 0.002$; Kruskal-Wallis test). There was no such trend in control mice. Because muscle atrophy is progressive in affected animals, this indicates a loss of NMJs in PMP22-Tg mice. The decline was particularly striking in the soleus, in which recognizable junctions at 24 weeks were less than 50% of the average value observed in control muscles ($p = 0.004$, Mann-Whitney U test). Whereas NMJ density was reduced at a similar rate in the EDL and soleus of the double-mutant mice between 8 and 16 weeks of age, further loss of NMJs in the EDL seemed to progress at a slower pace (Fig. 1E). Similar differences between the EDL and the soleus have been observed in other studies and might reflect intrinsic differences in NMJ maintenance between these muscles (28, 37, 38).

Quantification of NMJ profiles is summarized in Table 1. In all double-mutant muscles, the percentages of normal junctions were reduced and varied between 73% in the EDL at 16 weeks and 1.8% in the soleus at 24 weeks.

The double-mutant mouse EDL muscles showed more vacant NMJs than the soleus at all time points, that is, 2.2%, 1.2%, and 8.2% for the eighth, 16th, and 24th week intervals, respectively. Vacant NMJs were extremely rare in the mutant soleus, representing less than 1% of all NMJ muscle, a percentage that was similar to the amount of vacant NMJs in the control soleus. Vacant NMJs were not seen in the EDL of control mice. In contrast, the percentage of partially vacant NMJs was similar in the EDL and the soleus of PMP22-Tg mice and oscillated slightly over the study period; however, they never accounted more than 9.7% of NMJs in any muscle. The axonal branches overlying these junctions were often fragmented, and in some of these partially innervated NMJs, the presynaptic axon was also fragmented. This suggests that such junctions were undergoing denervation. At other junctions, the AChR-rich regions showed partial occupancy by a thin axon. This might indicate reinnervation, consistent with other studies (25, 39). Partially vacant NMJs associated with thick collapsed intrasynaptic terminals, as described in P0/MPZ-Tg mice (24), were seldom found.

The NMJs with sprouts were the most frequent category in muscles of double-mutant mice, and they increased steadily over time. The soleus exhibited more sprouting than the EDL at all time points. Specifically, 35%, 74%, and 94% of the NMJs in the soleus had sprouts at the 8, 16, and 24 weeks, respectively. Although the EDL was considered to be refractory to sprouting, NMJs with sprouting reached 45% of EDL NMJs at 6 months; terminal sprouts were often associated with a compact appearance of the NMJ. Occasionally, axonal outgrowth originated from a retraction bulb of the terminal axon (not shown). Moreover, nerve outgrowths not associated with pretzel-like NMJs contacted small unconnected AChR aggregates. This was particularly evident in older animals and in the soleus. The temporal sequence of these morphological changes suggests that stimuli that chronically induced nerve sprouting also promote NMJ disassembly.

Intramuscular Axons and Length

Earlier studies indicated that axonal sprouting occurred in hindlimb muscles of PMP22-Tg animals (29) (Figs. 2A–F). To quantify both the degree and progression of intramuscular axonal sprouting, we used a stereological probe and estimated the length of all presynaptic terminal axons and intrasynaptic branches and sprouts as a single unit within an ROI for each muscle. We reasoned that this approach would be sensitive as a measurement of sprouting if the growth of axons overpowered their loss. In young animals, the sprouting was predominantly confined to the NMJs (terminal sprouts), whereas collateral and terminal sprouts coexisted at later stages. Numerical data confirmed that the axon densities were higher in the double mutants versus the controls at all time points ($p = 0.004$, Mann-Whitney U test). There was also a significant trend of increasing axonal sprouts ($p = 0.001$, Kruskal-Wallis test) in both the soleus

FIGURE 2. Progressive sprouting of intramuscular nerves in PMP22-Tg mice. **(A–F)** Two-dimensional confocal images of extensor digitorum longus (EDL) **(A, C, E)** and soleus **(B, D, F)** muscles from *thy1*-YFP-16 **(A, B)** and PMP22-Tg, *thy1*-YFP-16 **(C–F)** mice. Axons are labeled green with yellow fluorescence protein (YFP); neuromuscular junctions (NMJs) are labeled red with α-bungarotoxin. Sprouting of motor nerve terminals (arrows) is apparent in the soleus and EDL muscles of PMP22-Tg, *thy1*-YFP-16 mice **(C–F)** across, but it is absent in the *thy1*-YFP-16 mice. **(G)** Histograms of the average length of terminal axons in the EDL and soleus muscles of PMP22-Tg, *thy1*-YFP-16 and *thy1*-YFP-16 controls. The lengths of terminal axons in the muscles of PMP22-Tg, *thy1*-YFP-16 were always longer than the lengths of terminal axons in the corresponding muscles of *thy1*-YFP-16 controls. With the exception of the *thy1*-YFP-16 soleus, there was a trend of increasing axonal sprouts during the study ($^{§,‡,¥}$ $p < 0.001$). Values are presented as mean ± SE. **(H)** Correlation plots between number of NMJs and axonal sprouts in the EDL and soleus muscles of PMP22-Tg, *thy1*-YFP-16 show an inverse correlation between the 2 parameters (EDL, $r = 0.7$, $p = 0.002$; soleus, $r = 0.8$; $p < 0.001$).

and EDL of the double-mutant animals during the study period (Fig. 2G). This increase in axonal sprouts inversely correlated with the number of NMJs in the soleus ($r = -0.8$; $p < 0.001$; Spearman rank correlation coefficient) and the EDL ($r = -0.7$; $p = 0.002$; Spearman rank correlation coefficient) of the double-mutant mice (Fig. 2H).

Because the ROI was not obtained by systematic random sampling, the preceding data might reflect an overestimation of axonal sprouts as a result of concomitant muscle atrophy in the double mutants. Therefore, we determined the volume of muscle where presynaptic terminal nerves, NMJs, and sprouts were found in a subset of muscles using the Cavalieri estimator (data not shown). Estimation of axonal sprouts after correction for change in muscle volume confirmed the sprouting behavior of intramuscular nerves in the soleus and the EDL of double-mutant mice. Compared with controls, these muscles scored an increase of axonal sprouts that ranged from 34% to 72% for the EDL and from 96% to 120% for the soleus.

Rotarod Study

The double-mutant animals underperformed on the rotarod test compared with the controls at all time points ($p < 0.05$; Mann-Whitney U test) (Fig. 3). The double-mutant animals showed deterioration between the ninth and 16th week interval ($p < 0.05$; Mann-Whitney U test). At the 23rd week interval, these animals were able to maintain their balance for a median of 85.7 seconds before falling off the rod, whereas the controls were balancing for a median of 244.9 seconds. The gender of the mice did not affect the outcome of these experiments.

Functional Deficits in the Innervation of Muscles

Chronically denervated muscle fibers express receptors for ACh outside the NMJ region, and their activation by bath-applied ACh causes dose-dependent muscle fiber contractures (34, 40). Soleus muscles of PMP22-Tg mice had higher ACh contracture amplitudes (range, 10–26 mN; median, 18 mN) versus controls (range, 2.4–9.1 mN; median, 6.15 mN; $p < 0.001$, Mann-Whitney U test), indicating considerable deficits in transmission (Table 2). Accordingly, there are atrophied small-diameter muscle fibers in the experimental muscles but not in controls (Table 2). Partial denervation led to reduced total muscle mass (4.8–11 mg; mean, 8.9 mg ± 2.0 SD for mutant muscles vs 9.0–13 mg; mean, 11.3 mg ± 1.3 SD for control muscles; $p < 0.01$, *t*-test). The ratios of these 2 independent measures of muscle denervation (ACh contracture amplitude and soleus muscle weight), were also significantly difference between the mutant and control muscles (range, 1.04–3.40 mN mg^{-1}; median, 2.12 mN mg^{-1} vs 0.21–0.84 mN mg^{-1}; median, 0.56 mN mg^{-1}; $p < 0.001$, Mann-Whitney U test) (Table 2). There was an inverse relation between the ratio ACh contracture per milligram and total muscle wet weight (Fig. 4).

Mutant muscles produced lower maximum tetanic forces (range, 20–163 mN; mean, 98 mN ± 47 SD vs 126–193 mN; mean, 159 mN ± 25 SD in control; $p < 0.005$, *t*-test, Table 2), which also correlated with muscle mass ($r^2 = 0.88$; data not shown). Stimulation of the ischiadic nerve failed to elicit muscle contractions in all 8 mutant muscles; stimulation of the much shorter soleus nerve was successful only in 5 of 8 preparations; this malfunction did not occur in any of the 10 control muscles. This result suggests failure of action potential propagation in the isolated nerve preparation and/or unusual mechanical fragility that allowed damage of mutant nerves during preparation.

Nerve-evoked muscle contractions resulted in similar values as direct stimulation despite the presence of denervated fibers in the mutant muscles (Table 2), suggesting that direct electrical stimulation as performed here does not cause contraction of all chronically denervated thin fibers. If there is contraction, their contribution to contractile force and weight is small. In 3 of 4 mutant mice, the degree of denervation differed in the different soleus muscles of the same animal. In general, there was generally variability in functional parameters in the mutant group than in the controls (Table 2).

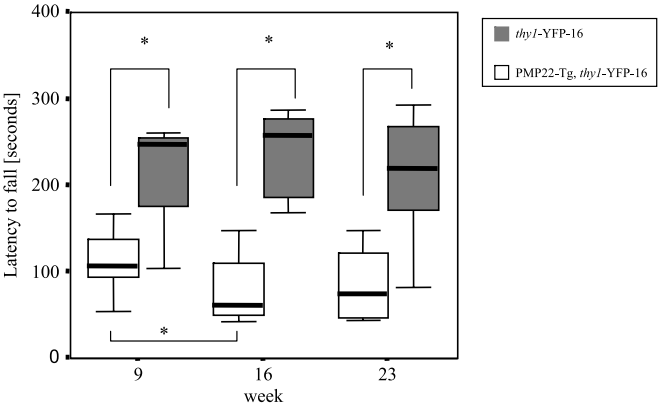

FIGURE 3. Box plot of results from the rotarod experiment. The PMP22-Tg, *thy1*-YFP-16 animals (n = 12) had impaired motor function at the start of the test compared with the *thy1*-YFP-16 controls (n = 10). There is further deterioration up to the 16th week after which it reached a plateau (*$p < 0.05$). The sample size of PMP22-Tg, *thy1*-YFP-16 mice was reduced to 7 at the 24th week. YFP, yellow fluorescence protein.

Muscle Atrophy Quantification

After the physiological recordings, soleus muscles were processed and analyzed using stereological probes to quantify muscle atrophy (Table 2). There were no differences in total numbers of soleus muscle fibers between PMP22 mutants and control mice, but the mutant muscles showed a moderate but significant reduction of both muscle area and average fiber caliber. Moreover, muscle fiber area distribution was remarkably different between PMP22-Tg mice and controls (Fig. 5). Whereas all control muscles displayed a normal distribution of fiber calibers, approximately 90% of control muscle fibers measured between 400 μm^2 and 1,200 μm^2. In contrast, the muscles of PMP22-Tg mice contained a significant proportion of atrophic fibers measuring less than 400 μm^2 (94%–27%; mean, 53% vs 9%–0%; mean, 4% in control muscles) (Fig. 5), and there were fewer fibers with areas between 600 μm^2 and 1,200 μm^2 (28%–2%; mean, 17%). Fibers of these calibers were the most numerous in controls (69%–54%; mean, 61%) (Fig. 5). In 2 of 3 instances in which a normal muscle cross-sectional area was preserved

TABLE 2. Isometric Contractile Properties, Weights, and Morphometry of Soleus Muscles of PMP22-Tg and Control Mice

Group	Muscle Weight, mg	ACh (0.2 mmol/L) Contracture, mN	ACh Contracture/ Muscle Weight, mN mg^{-1}	Maximum Tetanic Force Direct Stim, mN	Specific Force, N g^{-1}	Maximum Tetanic Force Indirect Stim, mN	Muscle Area, μm^2	No. Fibers	Mean Size of Fibers, μm^2
PMP22-Tg	9.8	11	1.12	113	12	—	755,166	755	684
	4.8	12	2.53	20	4.2	—	130,104	633	114
	8.1	20	2.43	57	7.0	52	408,123	726	405
	9.6	10	1.04	87	9.0	70	584,937	804	569
	10	19	1.90	138	14	137	977,557	889	791
	7.5	26	3.40	73	9.8	72	546,516	859	430
	10	24	2.33	129	13	102	582,804	824	452
	11	17	1.50	163	15	—	777,247	884	595
Mean ± SD	8.9 ± 2.0*	17 ± 5.9†	2.0 ± 0.8†	98 ± 47*	10 ± 3.5*	87 ± 33*	595,307 ± 256,032‡	797 ± 88	505 ± 206§
Non-PMP22-Tg	13	7.5	0.59	193	15	152	798,335	733	871
	13	5.8	0.46	179	14	151	1,036,350	815	970
	11	5.5	0.51	135	13	133	791,676	733	829
	12	2.4	0.21	179	15	157	816,423	842	788
	9.0	7.1	0.79	132	15	126	675,400	711	692
	9.4	5.7	0.61	126	13	115	731,944	722	713
	11	9.1	0.84	184	17	173	970,308	867	810
	11	8.8	0.80	174	16	153	956,172	862	774
	13	5.5	0.43	151	12	148	855,195	785	781
	12	6.5	0.53	136	11	123	754,019	668	737
Mean ± SD	11.3 ± 1.3	6.4 ± 1.9	0.6 ± 0.2	159 ± 25	14 ± 1.9	143 ± 18	838,582 ± 115,484	774 ± 70	797 ± 81

*$p < 0.01$, *t*-test; †$p < 0.001$; ‡$p < 0.05$; §$p < 0.01$, Mann-Whitney U test.
ACh, acetylcholine; mN, micronewton.

in the PMP22-Tg muscles, there was more hypertrophic fibers of greater than 1,600 μm^2. The third muscle contained a substantial proportion (64%) of medium-sized fibers. Correspondingly, these 3 muscles produced maximum tetanic tension upon direct stimulation that was close to control muscle values (Table 2).

DISCUSSION

We have demonstrated that NMJs are progressively lost in hindlimb skeletal muscles of PMP22-Tg mice. Concomitantly, there is a remarkable sprouting of motor axons as evidenced by increased axonal sprouts of motor terminal branches. These trends are inversely correlated in the mutant muscles. The loss of mature NMJs is likely a consequence of 3 ongoing denervation, instability of sprouting NMJs, and eventual failure of axonal outgrowth to sustain reinnervation.

Loss of Mature NMJs

As PMP22- Tg mice age, the number of mature NMJs declines. The soleus consistently shows greater loss of NMJs than the EDL, as in other experimental paradigms such as denervation and paralysis induced by botulinum toxin A (37). This has been considered to reflect greater stability and independence from activity-dependent maintenance of the postsynaptic apparatus on the EDL compared with the soleus. In this respect, it is interesting to note that the EDL of PMP22-Tg mice seems to have more vacant NMJs than the soleus at all time points. Recently, neuromuscular synaptogenesis has also been shown to differ between these 2 muscles in mice. It has been proposed that postsynaptic differentiation processes intrinsic to skeletal muscles influences the formation of NMJs during development as well as their maintenance in the adult (36). The higher density of NMJs in young PMP22-Tg mice compared with controls may be a consequence of muscle atrophy in the former animals. Indeed, fascicular muscle atrophy has been detected in 70-day-old PMP22-Tg mice (17). It is unlikely that polyinnervation is responsible for the increased density of

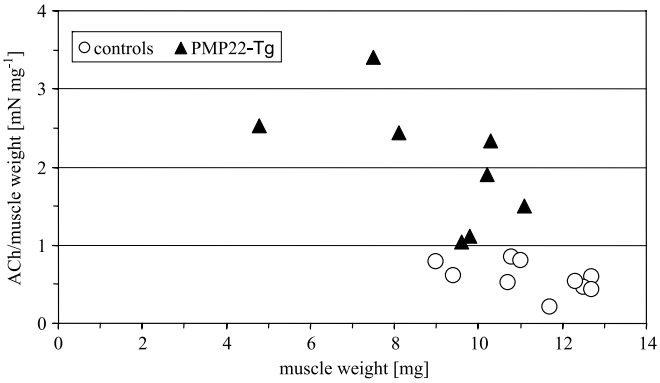

FIGURE 4. Acetylcholine (ACh) sensitivity of isolated soleus muscle fibers of PMP22-Tg mice. The ACh contracture amplitudes per wet weight of soleus muscles showed higher values in PMP22-Tg mice compared with controls, suggesting denervated and atrophied muscle fibers in the PMP22-Tg mice.

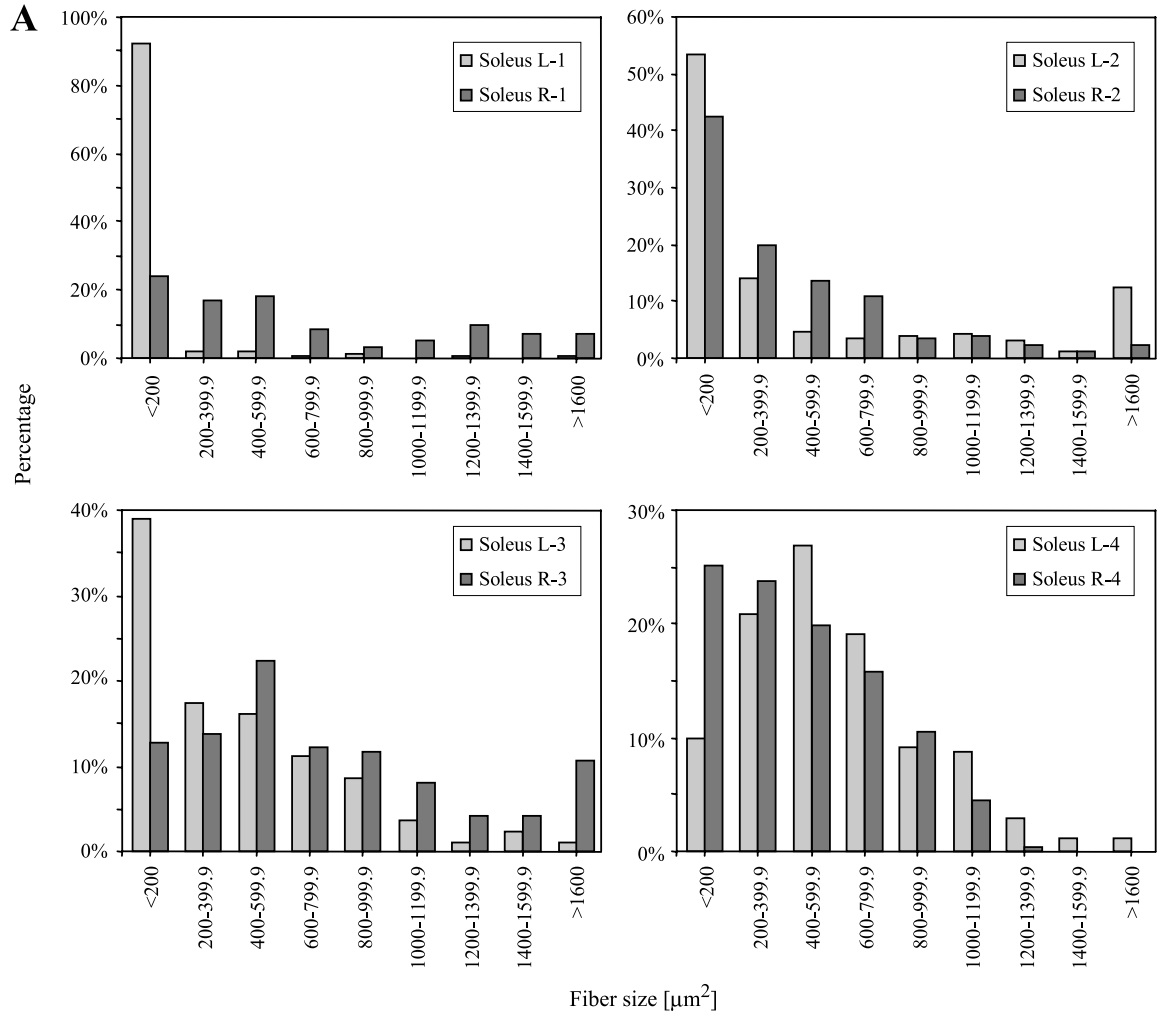

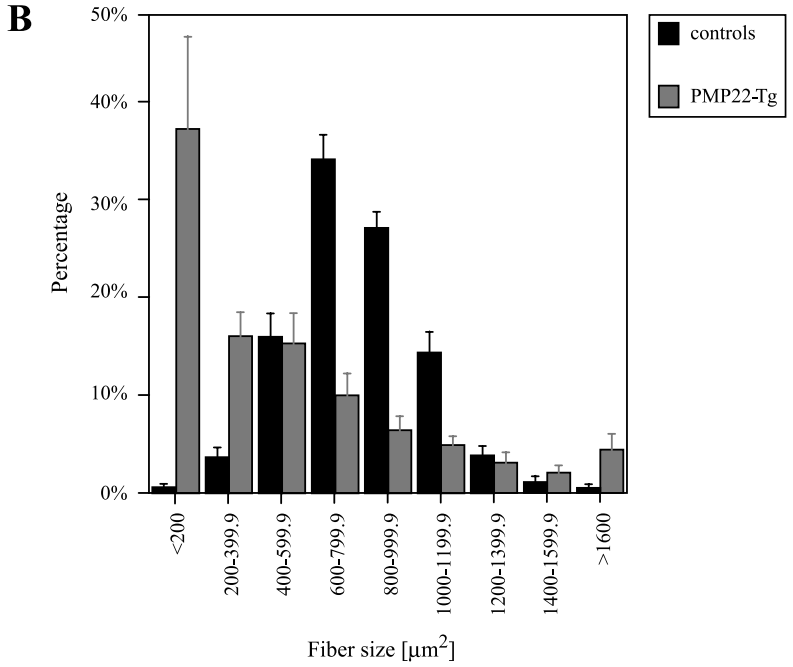

junctions because only en plaque NMJs with pretzel-like morphology were quantified. Rarely, 2 innervated en plaque NMJs coexist in the same muscle fiber; polyinnervated neonatal muscle fibers possess a single NMJ that is innervated by more than 1 axon (41). Some extrafusal fibers of the extraocular muscles have distributed innervation with multiple grapelike endings but a single en plaque NMJ (42). Furthermore, newly reinnervated muscle fibers may be polyinnervated by 2 axons that converge to the same NMJ (43). However, we cannot completely rule out the possibility that the old vacant NMJ and a newly assembled reinnervated NMJ are present together on some muscle fibers.

Denervated NMJs were identified in the EDL of PMP22 mutants. In contrast, the soleus of the PMP22-Tg animals did not have more denervated junctions than the soleus of controls. Because the soleus is particularly vulnerable to processes that impair NMJ stability including denervation (44), the denervated NMJs in the soleus might have been removed if they were not rapidly reinnervated. Remarkably, the percentage of partially vacant NMJs was similar in the soleus and in the EDL of PMP22-Tg mice, supporting this conclusion. Alternatively, only motor neurons innervating the EDL, a fast-twitch muscle, were losing their terminal axons. Indeed, distinct subpopulations of motor neurons show different susceptibilities to disease in a mouse model of amyotrophic lateral sclerosis (39). In this model, axons of fast-twitch and fast-fatigable motor neurons are more vulnerable than axons of fast twitch and fatigue-resistant motor neurons, whereas slow-twitch motor neurons are relatively refractory to the disease process and sprout to reinnervate denervated end plates (38, 45). Although the present study does not provide information of how denervation occurs, the identification of axonal fragmentation in some partially vacant NMJs suggests axonal degeneration. As reported by others, the early involvement of terminal branches of motor axons supports distal axonopathy as a disease mechanism (24).

Growth of Intramuscular Axons

Although denervation of end plates remained low across the study period, overgrowth of axons in the EDL and soleus (as judged by axonal sprouts and percentage of sprouting NMJs) increased with age in PMP22-Tg mice. This implies that the axons of these mice can regenerate. Despite severe denervation, 3 mouse models of motor neuron disease (i.e. SOD1[G93A], Mnd, and pmn) show limited motor axon sprouting (45). Moreover, axon growth in an amyotrophic lateral sclerosis model is mostly confined to collateral sprouts, probably initiated at nodes of Ranvier (39). In contrast, PMP22-Tg mice show strong terminal sprouting of the NMJs, a phenomenon that is also present in P0-Tg mice (24) and Trembler mice (28). Partial denervation and paralysis induced by blockade of synaptic transmission are potent inducers of motor axon overgrowth (46), but there are differences in the amount and type of sprout growth induced. Denervation stimulates nodal sprouts originating from nodes of Ranvier as well as terminal sprouts, whereas paralysis preferentially induces terminal sprouts. In addition, direct stimulation of the muscle suppresses terminal sprouting of partially denervated and paralyzed muscle fibers, but nodal sprouting is unaffected (47, 48). Muscle paralysis induced by chronic administration of botulinum toxin A, a toxin that blocks calcium-dependent transmitter release, has a pronounced effect on the NMJs of some muscles, whereas other muscles are resistant. Thus, repeated applications of toxin to the soleus leads to pronounced NMJ remodeling and sprouting; the EDL is unaffected (37). In marked contrast, the EDL of PMP22-Tg mice sprouts strongly, albeit less than the soleus. The remodeling of NMJs induced by chronic paralysis involves terminal sprouting of NMJs, followed by withdrawal of intrasynaptic terminals, loss of postsynaptic AChR and growing of collateral sprouts that preferentially originate from the distal segment of the terminal axon close to the NMJ. This sequence of events is remarkably similar to what we observed in the muscles of PMP22-Tg mice, raising the question of whether synaptic dysfunction participates in the development of the neuromuscular pathology. Indeed, impaired synaptic function has been reported in P0-Tg and in Trembler mice. Although many of the functional alterations observed in those mice are attributable to atrophy and denervation-like pathology of muscle fibers, intermittent conduction block affecting whole motor units has been implicated as an additional determinant of the sprouting phenotype in both mouse strains (24, 28).

In addition to their essential role in the development, maturation, and regeneration of axons in peripheral nerves, SCs are important in the formation, function, and maintenance of the NMJs (49). Terminal SCs cover nerve terminals and are in close proximity to the NMJ, where they sense neurotransmitter release and can influence short-term plasticity (50, 51). They are induced by denervation and paralysis to extend processes that guide regenerating axons as well as terminal sprouts to reinnervate denervated NMJs (52, 53). We found that there was almost 100% colocalization of SC processes to the YFP+ axon in the soleus, EDL, and also the gastrocnemius muscles, suggesting that PMP22 overexpression does not compromise the guiding function of SCs (data not shown). A strong progressive intramuscular sprouting response seems to be common to PMP22-Tg mice as well as P0-Tg mice and Trembler mice, all of which are affected by a dysmyelinating neuropathy. Lack of myelin, the presence of which is known to inhibit axonal growth, may facilitate sprouting, but it is presently unclear whether dysmyelination does or does not play any role in these processes.

Rotarod Performance

Motor functions in young PMP22-Tg animals were already severely impaired when they were first tested in the

FIGURE 5. Atrophy of skeletal muscle fibers in PMP22-Tg mice. **(A)** Histograms showing the area distribution of skeletal muscle fibers in the left and right soleus muscles of individual PMP22-Tg mice. Note the presence of hypertrophic fibers (>1,600 μm^2) in 1R, 2L, 3R, and 4L. L, left; R, right. **(B)** Histogram representing the mean fiber area distribution of PMP22-Tg (n = 8) and control (n = 10) mice. Muscle fibers measuring less than 400 μm^2 account for 53% of skeletal muscle fibers in the soleus of PMP22-Tg mice as opposed to only 4% of skeletal muscle fibers in the soleus of controls. Values are presented as mean ± SE.

rotarod experiments. Their performances were still remarkable because the rotarod involves a complex array of bodily responses to stay balanced on the rotating cylinder (54). From the eighth to the 24th week of the study period, we did not see any appreciable changes in terms of behaviors, and the declining performance in the rotarod seemed to be stabilized after the 16th week. The reasons for this observation remain unclear, but although the number of NMJs steadily declined in the soleus of PMP22-Tg mice across the study period, the EDL showed a relative stabilization after the 16th week. We speculate that the EDL, a fast-twitch muscle and a dorsiflexor, may play a more important role than the slow-twitch plantar flexor soleus during the rotarod test. Indeed, partial denervation of the EDL results in tonic activity of the remaining motor units during standing and significantly alters the pattern of activity of the muscle during locomotion (26, 55). In contrast, the soleus can function relatively well even when it is innervated by only a third of its original motor neuron pool (56). By analogy, this might explain the prevalence of foot drop as a consequence of dysfunctional dorsiflexors in CMT1A patients (6).

Electrophysiological Measurements

The present results clearly show different degrees of chronic denervation in the mutant muscles. The presence of enhanced sensitivity to ACh of isolated soleus muscles, together with the loss in muscle mass and the appearance of small-diameter fibers in the PMP22-Tg muscles, strongly indicates that they were partially denervated. Because denervation seems to proceed with time, a mixture of fully innervated to completely denervated values are simultaneously present in a muscle, rendering the comparison of contractile strength elicited via direct and indirect (nerve) stimulation (degree of innervation of a muscle) as unreliable.

The difference in the amount of denervation among age-matched mutant mice was considerable and included differences between the 2 solei of the same animal. The reason for this is unknown, but different loading with body weight of the 2 limbs during running might be a determining factor. Our observation of enhanced fragility of the nerve, 3 of 8 preparations were damaged in the course of dissecting the preparation in experimental mice, but none of 10 control muscles supports this notion.

In conclusion, our present results show that in this as in other models, the NMJ is systematically vulnerable to inherited myelin disorders of the PNS. The remarkable sprouting response of intramuscular motor terminals indicates that dysmyelinated axons are able to regenerate. Yet they cannot prevent the substantial loss of NMJs and the severe muscle atrophy found at 6 to 8 months of age in the mutant mice. Synaptic vulnerability is now emerging as a common pathogenic mechanism across several neurodegenerative diseases (57), and the addition of PNS myelin diseases would thus broaden the spectrum of disorders in which synaptic connectivity is compromised and might benefit from therapeutic strategies aimed to protect the synaptic compartment. However, it remains to be determined to what extent the NMJ is altered in CMT1 patients.

ACKNOWLEDGMENTS

The authors thank L.M. Cruz-Orive (University of Cantabria, Cantabria, Spain) and M. Geiser (University of Bern, Bern, Switzerland) for their advice concerning the use of design-based stereology. The authors thank U. Suter (ETH-Zurich, Zurich, Switzerland) for valuable comments on the manuscript and J.-P. Gabriel (University of Fribourg, Fribourg, Switzerland) for his input concerning the use of statistics. The authors also thank D. Glass (University of Bonn, Bonn, Germany) and D. Uldry (University of Fribourg, Fribourg, Switzerland) for their expert technical contributions.

REFERENCES

1. Grandis M, Shy ME. Current therapy for Charcot-Marie-Tooth disease. Curr Treat Options Neurol 2005;7:23–31
2. Shy ME, Rose MR. Charcot-Marie-Tooth disease impairs quality of life: Why? And how do we improve it? Neurology 2005;65:790–91
3. Nelis E, Van Broeckhoven C, De Jonghe P, et al. Estimation of the mutation frequencies in Charcot-Marie-Tooth disease type 1 and hereditary neuropathy with liability to pressure palsies: A European collaborative study. Eur J Hum Genet 1996;4:25–33
4. Wise CA, Garcia CA, Davis SN, et al. Molecular analyses of unrelated Charcot-Marie-Tooth (CMT) disease patients suggest a high frequency of the CMTIA duplication. Am J Hum Genet 1993;53:853–63
5. Thomas PK, Marques W Jr, Davis MB, et al. The phenotypic manifestations of chromosome 17p11.2 duplication. Brain 1997;120(Pt 3): 465–78
6. Vinci P, Perelli SL. Footdrop, foot rotation, and plantarflexor failure in Charcot-Marie-Tooth disease. Arch Phys Med Rehabil 2002;83:513–16
7. Garcia A, Combarros O, Calleja J, et al. Charcot-Marie-Tooth disease type 1A with 17p duplication in infancy and early childhood: A longitudinal clinical and electrophysiologic study. Neurology 1998;50: 1061–67
8. Killian JM, Tiwari PS, Jacobson S, et al. Longitudinal studies of the duplication form of Charcot-Marie-Tooth polyneuropathy. Muscle Nerve 1996;19:74–78
9. Roa BB, Garcia CA, Suter U, et al. Charcot-Marie-Tooth disease type 1A. Association with a spontaneous point mutation in the *PMP22* gene. N Engl J Med 1993;329:96–101
10. Valentijn LJ, Baas F, Wolterman RA, et al. Identical point mutations of PMP-22 in Trembler-J mouse and Charcot-Marie-Tooth disease type 1A. Nat Genet 1992;2:288–91
11. Gabreels-Festen AA, Gabreels FJ, Jennekens FG, et al. The status of HMSN type III. Neuromuscul Disord 1994;4:63–69
12. Gabreels-Festen AA, Bolhuis PA, Hoogendijk JE, et al. Charcot-Marie-Tooth disease type 1A: Morphological phenotype of the 17p duplication versus PMP22 point mutations. Acta Neuropathol 1995;90: 645–49
13. Thomas PK, King RH, Small JR, et al. The pathology of Charcot-Marie-Tooth disease and related disorders. Neuropathol Appl Neurobiol 1996; 22:269–84
14. Hattori N, Yamamoto M, Yoshihara T, et al. Demyelinating and axonal features of Charcot-Marie-Tooth disease with mutations of myelin-related proteins (PMP22, MPZ and Cx32): A clinicopathological study of 205 Japanese patients. Brain 2003;126:134–51
15. Ericson U, Ansved T, Borg K. Charcot-Marie-Tooth disease—muscle biopsy findings in relation to neurophysiology. Neuromuscul Disord 1998; 8:175–81
16. Huxley C, Passage E, Manson A, et al. Construction of a mouse model of Charcot-Marie-Tooth disease type 1A by pronuclear injection of human YAC DNA. Hum Mol Genet 1996;5:563–69
17. Magyar JP, Martini R, Ruelicke T, et al. Impaired differentiation of Schwann cells in transgenic mice with increased *PMP22* gene dosage. J Neurosci 1996;16:5351–60
18. Robertson AM, Perea J, McGuigan A, et al. Comparison of a new pmp22 transgenic mouse line with other mouse models and human patients with CMT1A. J Anat 2002;200:377–90

19. Sereda M, Griffiths I, Puhlhofer A, et al. A transgenic rat model of Charcot-Marie-Tooth disease. Neuron 1996;16:1049–60
20. Huxley C, Passage E, Robertson AM, et al. Correlation between varying levels of PMP22 expression and the degree of demyelination and reduction in nerve conduction velocity in transgenic mice. Hum Mol Genet 1998;7:449–58
21. Adlkofer K, Martini R, Aguzzi A, et al. Hypermyelination and demyelinating peripheral neuropathy in Pmp22-deficient mice. Nat Genet 1995;11:274–80
22. Sancho S, Magyar JP, Aguzzi A, et al. Distal axonopathy in peripheral nerves of PMP22-mutant mice. Brain 1999;122(Pt 8):1563–77
23. Frei R, Motzing S, Kinkelin I, et al. Loss of distal axons and sensory Merkel cells and features indicative of muscle denervation in hindlimbs of P0-deficient mice. J Neurosci 1999;19:6058–67
24. Yin X, Kidd GJ, Pioro EP, et al. Dysmyelinated lower motor neurons retract and regenerate dysfunctional synaptic terminals. J Neurosci 2004; 24:3890–98
25. Wernig A, Carmody JJ, Anzil AP, et al. Persistence of nerve sprouting with features of synapse remodelling in soleus muscles of adult mice. Neuroscience 1984;11:241–53
26. Slawinska U, Tyc F, Kasicki S, et al. Time course of changes in EMG activity of fast muscles after partial denervation. Exp Brain Res 1998; 120:193–201
27. Wernig A, Herrera AA. Sprouting and remodelling at the nerve-muscle junction. Prog Neurobiol 1986;27:251–91
28. Gale AN, Gomez S, Duchen LW. Changes produced by a hypomyelinating neuropathy in muscle and its innervation. Morphological and physiological studies in the Trembler mouse. Brain 1982;105:373–93
29. Maier M, Berger P, Suter U. Understanding Schwann cell-neurone interactions: The key to Charcot-Marie-Tooth disease? J Anat 2002;200: 357–66
30. Feng G, Mellor RH, Bernstein M, et al. Imaging neuronal subsets in transgenic mice expressing multiple spectral variants of GFP. Neuron 2000;28:41–51
31. Mouton PR, Gokhale AM, Ward NL, et al. Stereological length estimation using spherical probes. J Microsc 2002;206:54–64
32. Schmitz C, Hof PR. Design-based stereology in neuroscience. Neuroscience 2005;130:813–31
33. Irintchev A, Draguhn A, Wernig A. Reinnervation and recovery of mouse soleus muscle after long-term denervation. Neuroscience 1990;39:231–43
34. Wernig A, Zweyer M, Irintchev A. Function of skeletal muscle tissue formed after myoblast transplantation into irradiated mouse muscles. J Physiol 2000;522(Pt 2):333–45
35. Norreel JC, Jamon M, Riviere G, et al. Behavioural profiling of a murine Charcot-Marie-Tooth disease type 1A model. Eur J Neurosci 2001;13: 1625–34
36. Pun S, Sigrist M, Santos AF, et al. An intrinsic distinction in neuromuscular junction assembly and maintenance in different skeletal muscles. Neuron 2002;34:357–70
37. Santos AF, Caroni P. Assembly, plasticity and selective vulnerability to disease of mouse neuromuscular junctions. J Neurocytol 2003;32:849–62
38. Pun S, Santos AF, Saxena S, et al. Selective vulnerability and pruning of phasic motoneuron axons in motoneuron disease alleviated by CNTF. Nat Neurosci 2006;9:408–19
39. Schaefer AM, Sanes JR, Lichtman JW. A compensatory subpopulation of motor neurons in a mouse model of amyotrophic lateral sclerosis. J Comp Neurol 2005;490:209–19
40. Witzemann V, Schwarz H, Koenen M, et al. Acetylcholine receptor epsilon-subunit deletion causes muscle weakness and atrophy in juvenile and adult mice. Proc Natl Acad Sci U S A 1996;93:13286–91
41. Lichtman JW, Colman H. Synapse elimination and indelible memory. Neuron 2000;25:269–78
42. Sadeh M, Gilad R, Dabby R, et al. Apparent weakness of ulnar-innervated muscles in radial palsy. Neurology 2004;62:1424–25
43. Rich MM, Lichtman JW. In vivo visualization of pre- and postsynaptic changes during synapse elimination in reinnervated mouse muscle. J Neurosci 1989;9:1781–805
44. Brown MC, Hopkins WG, Keynes RJ, et al. A comparison of early morphological changes at denervated and paralyzed endplates in fast and slow muscles of the mouse. Brain Res 1982;248:382–86
45. Frey D, Schneider C, Xu L, et al. Early and selective loss of neuromuscular synapse subtypes with low sprouting competence in motoneuron diseases. J Neurosci 2000;20:2534–42
46. Schafer R, Wernig A. Polyclonal antibodies against NCAM reduce paralysis-induced axonal sprouting. J Neurocytol 1998;27:615–24
47. Brown MC, Holland RL, Hopkins WG. Motor nerve sprouting. Ann Rev Neurosci 1981;4:17–42
48. Brown WF, Feasby TE. Conduction block and denervation in Guillain-Barré polyneuropathy. Brain 1984;107(Pt 1):219–39
49. Koirala S, Reddy LV, Ko CP. Roles of glial cells in the formation, function, and maintenance of the neuromuscular junction. J Neurocytol 2003;32:987–1002
50. Colomar A, Robitaille R. Glial modulation of synaptic transmission at the neuromuscular junction. Glia 2004;47:284–89
51. Rousse I, Robitaille R. Calcium signaling in Schwann cells at synaptic and extra-synaptic sites: Active glial modulation of neuronal activity. Glia 2006;54:691–99
52. Son YJ, Thompson WJ. Nerve sprouting in muscle is induced and guided by processes extended by Schwann cells. Neuron 1995;14: 133–41
53. Son YJ, Thompson WJ. Schwann cell processes guide regeneration of peripheral axons. Neuron 1995;14:125–32
54. Crawley JN. Behavioral phenotyping of transgenic and knockout mice: Experimental design and evaluation of general health, sensory functions, motor abilities, and specific behavioral tests. Brain Res 1999;835:18–26
55. Tyc F, Vrbova G. The effect of partial denervation of developing rats fast muscles on their motor unit properties. J Physiol 1995;482:651–60
56. Slawinska U, Navarrete R, Kasicki S, et al. Motor activity patterns in rat soleus muscle after neonatal partial denervation. Neuromuscul Disord 1995;5:179–86
57. Wishart TM, Parson SH, Gillingwater TH. Synaptic vulnerability in neurodegenerative disease. J Neuropathol Exp Neurol 2006;65:733–39

